Check for updates

Advanced Optical Materials

ADVANCED OPTICAL MATERIALS
www.advopticalmat.de

RESEARCH ARTICLE OPEN ACCESS

Self-Powered Visible-Blind Graphene/NiO/ZnO UV-C Photodiodes

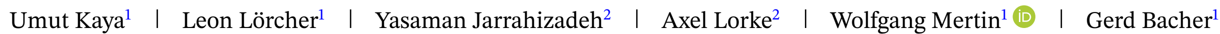
Umut Kaya[1] | Leon Lörcher[1] | Yasaman Jarrahizadeh[2] | Axel Lorke[2] | Wolfgang Mertin[1] | Gerd Bacher[1]

[1]Werkstoffe Der Elektrotechnik and CENIDE, Universität Duisburg-Essen, Duisburg, Germany | [2]Fakultät für Physik and CENIDE, Universität Duisburg-Essen, Duisburg, Germany

Correspondence: Gerd Bacher (gerd.bacher@uni-due.de)

Received: 18 March 2026 | **Revised:** 27 May 2026 | **Accepted:** 15 June 2026

Keywords: graphene | NiO | self-powered | UV-C photodiode | visible-blind | ZnO

ABSTRACT

Continuous monitoring of deep-ultraviolet (UV-C) radiation is crucial for applications ranging from germicidal sterilization to secure communications. While metal-oxide semiconductors offer a scalable alternative to costly SiC or AlGaN technologies, their performance is typically bottlenecked by the lack of robust -p-type layers and UV-C transparent electrodes. In this work, we demonstrate a high-performance, self-powered UV-C photodiode that overcomes these limitations through a fully scalable architecture. We address the transparency constraint by utilizing graphene, directly synthesized via low-temperature plasma-enhanced chemical vapor deposition on sapphire, as a highly transparent hole-collecting anode. A vertical p-NiO/n-ZnO heterojunction is subsequently fabricated via magnetron sputtering, capped with a UV-C reflective aluminum mirror. By tuning the oxygen stoichiometry during sputtering, we induce nickel vacancy acceptors that significantly enhance the p-NiO conductivity and junction quality. Operating in self-powered mode, the device delivers a peak responsivity of 7.9 mA/W under 261 nm excitation and a UV-to-visible rejection ratio of $> 10^2$. It also exhibits rapid response times <50 ms and an exceptional ON/OFF ratio of 10^4. These findings establish graphene integrated with optimized metal oxides as a viable route toward low-cost, large-area UV-C optoelectronics.

1 | Introduction

The deep-ultraviolet (UV-C) spectral band (200–280 nm) has become a focal point of modern optoelectronics, driven by critical applications like global health monitoring and secure communications [1–4]. In particular, the rapid adoption of UV-C light-emitting diodes (LEDs) for germicidal irradiation – essential for water purification and surface sterilization – has created an urgent demand for robust, large-area detectors capable of precise dosimetry [5–7]. However, accurately monitoring these high-energy photons remains a technological challenge, since ideal detectors must combine high responsivity with exceptional durability against high-energy radiation, all while maintaining low dark currents to resolve weak signals in noise-sensitive environments [8, 9]. These stringent requirements are optimally addressed by pn-junction photodiodes (PDs) designed for zero-bias, i.e., self-powered, operation. By relying entirely on the heterojunction's built-in electric field for charge carrier separation, these devices inherently suppress bias-induced dark currents and thermal noise. This photovoltaic mode of operation maximizes the signal-to-noise ratio for detecting weak UV-C signals, while simultaneously eliminating the need for external power supplies in remote or portable dosimetry systems [10].

Conventional solutions often rely on complex device architectures to circumvent intrinsic material limitations. Silicon (Si) based PDs benefit from mature fabrication processes but lack intrinsic visible-blindness, necessitating costly external filters to

This is an open access article under the terms of the Creative Commons Attribution License, which permits use, distribution and reproduction in any medium, provided the original work is properly cited.
© 2026 The Author(s). *Advanced Optical Materials* published by Wiley-VCH GmbH

reject visible light [11]. Conversely, wide-bandgap semiconductors like silicon carbide and AlGaN deliver exceptional UV-selectivity and radiation hardness, yet their widespread adoption is impeded by intrinsic material and processing challenges. Silicon carbide, as an indirect bandgap semiconductor, has a fundamentally low optical absorption coefficient in the deep-UV regime, which necessitates the growth of bulky layers to achieve sufficient quantum efficiency [12]. Meanwhile, Al-rich AlGaN layers suffer from notoriously low p-doping efficiency, diminishing the p-conductivity and thus device performance [13].

In contrast to these constraints, metal oxide semiconductors have emerged as a scalable and cost-effective alternative for wide-bandgap photodetectors [8]. While (*n*-type) Gallium Oxide (Ga_2O_3) offers the strict solar-blindness preferable for outdoor operation, achieving device-grade quality via sputtering remains challenging as controlling the several polymorphic phases is not trivial, resulting in inhomogeneities in electrical performance [14]. For indoor applications – specifically germicidal sterilization – strict solar rejection is not required [15]. In this context, *n*-type Zinc Oxide (ZnO) presents a superior alternative, combining sufficient visible-blindness with facile synthesis and excellent electron transport properties [16–18]. The primary bottleneck, however, lies in the p-side, as reliable *p*-type conductivity is historically difficult to achieve in metal oxides [19]. Nickel oxide (NiO) stands out as the only viable wide-bandgap *p*-type metal oxide due to its partially filled 3d orbital and hence higher valence band energy compared to other metal oxides [20].

Current literature on p-NiO/n-ZnO metal oxide PDs that focus on UV-C absorption is scarce. Rahman et al. achieved exceptionally high responsivities of 167 A/W with 253 nm excitation and − 30 V applied voltage [21]. Other groups have shown similarly high performances with 5.77 and 291 A/W, but with UV-A excitation (365 nm) at − 2 V applied voltage [22, 23]. However, neither of these studies demonstrate self-powered operation (0 V). Also, the given responsivities indicate that additional gain mechanisms known from photoconductors must be at play, since for pure PDs the maximum quantum efficiency $\eta = 1$ (every photo-generated charge carrier contributes to the photocurrent) limits the wavelength-dependent responsivity. For example, in the UV-regime between $\lambda = 250 - 380$ nm the theoretical responsivity limit is expected to be $R_{max} \approx \eta e \frac{\lambda}{hc} \approx 0.20 - 0.31$ A/W. Focusing on self-powered UV-C PDs only, responsivities up to ~30 mA/W at the expense for slower response times ~100 − 500 ms have been reported [24, 25]. These devices however, are based on non-scalable and challenging processing methods [24, 26] as well as non-abundant and potentially harmful materials (rare earth oxides [27], perovskites [28]). In addition, a critical yet often overlooked bottleneck for current approaches is the top electrode: standard transparent conductive oxides like Indium Tin Oxide (ITO) become opaque in the deep UV regime (<350 nm) [29], forcing devices to rely on metal finger electrodes on the top-side that shadow the active area and limit detector efficiency.

To address all these limitations, we propose a unique device architecture constructed upon a sapphire substrate, which serves a dual function: it acts as a UV-C transparent window for backside illumination and, crucially, provides an ideal template for the direct growth of graphene [30]. Synthesized via low-temperature plasma-enhanced chemical vapor deposition (PECVD), graphene serves as a hole-collection electrode, combining high electrical conductivity due to its sp^2-hybridized carbon lattice with exceptional UV-C transparency exceeding 90% [29]. Deposited onto this transparent graphene anode is a UV-C absorbing p-NiO/n-ZnO heterojunction, realized via a highly-scalable and cost-effective sputtering process. This active region bypasses the doping challenges of AlGaN by combining the naturally leverageable hole conductivity of NiO [31] with the high electron mobility of ZnO [16]. Lastly, the stack is capped with an Aluminum (Al) electrode acting as a UV-C reflective mirror [32], which allows the optical recycling of non-absorbed photons and hence a thinning of the metal-oxide heterojunction to shorten the carrier extraction paths.

2 | Results

The main steps of our UV-C PD processing chain (graphene growth, metal oxide sputtering, and metallization) are shown schematically in Figure 1a–c. After cleaning the c-plane sapphire substrate, graphene is grown directly on top via a low-temperature PECVD process (s. Figure 1a and Figure S1). Methane (CH_4) is used as a precursor alongside nitrogen (N_2) as the carrier gas. Once the plasma is ignited, CH_4 is decomposed into CH_x (x = 0–3) species, which adsorb on the sapphire surface and contribute to the nucleation and growth of the graphene film [30]. Due to the dielectric nature of the sapphire substrate, positive charges are able to accumulate on its surface and prevent further growth by shielding the CH_x ions in the plasma from reaching the substrate surface. To mitigate this surface charge build-up, the DC-plasma is pulsed with a certain frequency *f*, which changes the sign of the applied voltage and hence allows for the compensation of build-up charge and the continuation of graphene growth on the sapphire surface (Figure S2).

Typical characterization methods of graphene include x-ray photoelectron spectroscopy (XPS) and Raman spectroscopy. The prior yields the C1s spectrum of the grown graphene (see Figure 1d), which verifies the strong presence of sp^2-carbon in the as-grown graphene layer. Often, the sp^3-carbon related peak is also fitted into the C1s spectrum at slightly higher binding energies ($\Delta E \sim 1$ meV). However, the distinction is challenging due to the significant overlap of both signals. Instead, the C KLL Auger peak in Figure 1e can be used to derive the so-called D-parameter, which is highly sensitive to the electronic structure of the carbon thin film. Here, an approximate value of D ~ 21.5 eV (s. Figure 1f) confirms that the PECVD-grown graphene film overwhelmingly consists of graphite-like sp^2-hybridized carbon atoms, compared to practically non-existent sp^3-carbon (D ~13.7 eV) [33].

Figure 1g shows the Raman spectra of directly grown graphene films as a function of plasma frequency ranging from 1 to 100 kHz (blue to violet). The successful growth of graphene can be derived from the presence of all the signature Raman peaks of graphene (D, G, and 2D). Here, the G- and 2D-peaks are the most important ones since they describe the sp^2-hybridized carbon atom arrangement and the far-range order of the graphene crystal. Since monolayer graphene typically shows $I_{2D}/I_G > 2$ [34], our value $I_{2D}/I_G \sim 1$ in combination with absorption measurements in the visible range (Figure S3) hints toward 2 – 6 layers of graphene (few-layer graphene, *FLG*) [35]. As expected from a plasma-driven

21951071, 0, Downloaded from https://advanced.onlinelibrary.wiley.com/doi/10.1002/adom.71412 by Universitaet Duisburg-Essen, Wiley Online Library on [02/07/2026]. See the Terms and Conditions (https://onlinelibrary.wiley.com/terms-and-conditions) on Wiley Online Library for rules of use; OA articles are governed by the applicable Creative Commons License

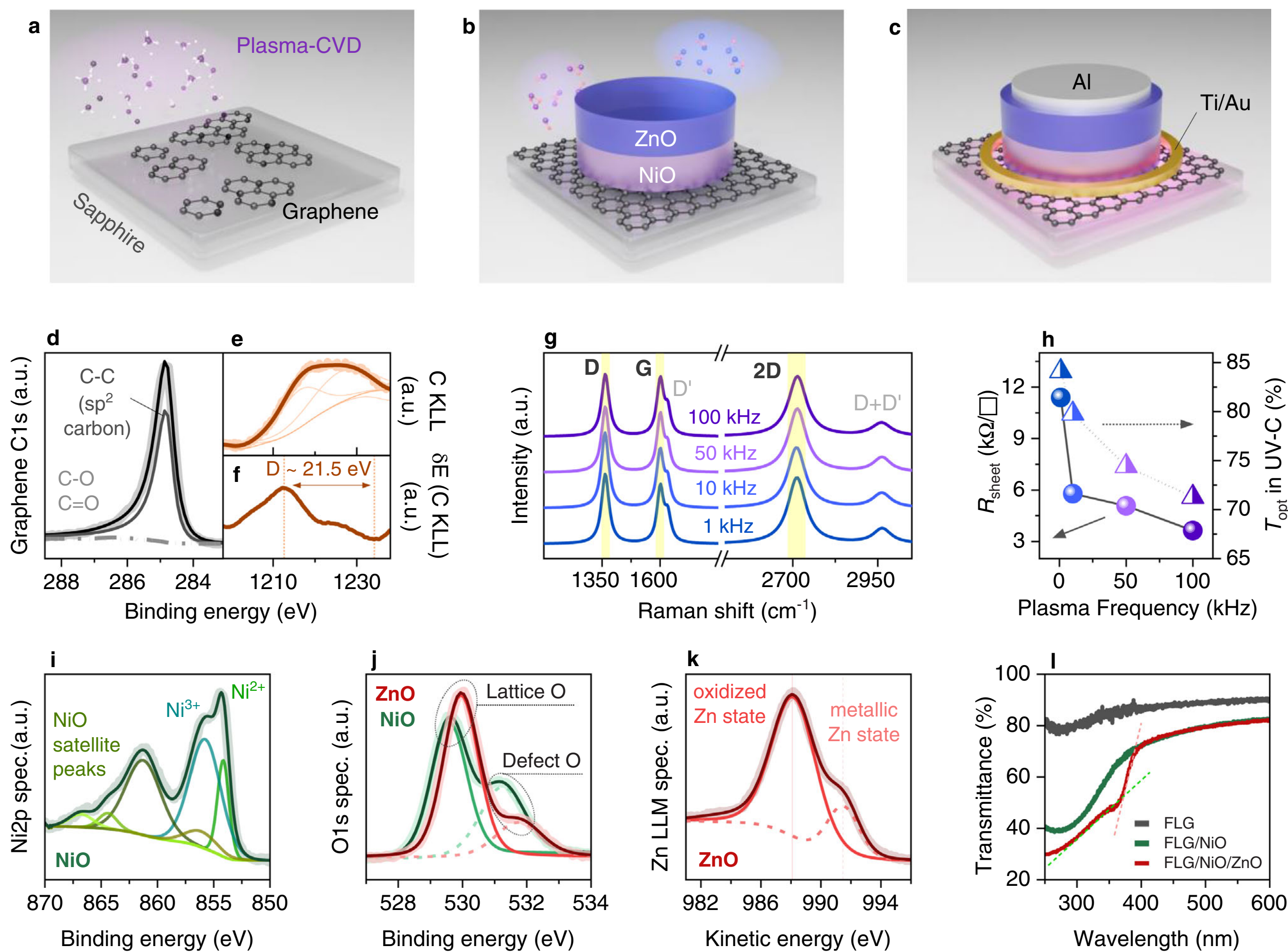

FIGURE 1 | Fully scalable process flow of a graphene/metal-oxide based UV-C photodiode. (A) Schematic visualization of graphene growth via PECVD. (b) Sputtering of a NiO/ZnO heterojunction directly onto graphene and (c) metallization of Ti/Au bottom electrode and Al top electrode acting as UV-C mirror using optical lithography. (d) C1s spectrum of graphene demonstrating sp^2-hybridization of the grown graphene. (e) C KLL Auger spectrum and (f) its derivative to obtain the D-parameter, which contains information about graphene's electronic structure. (g) Raman spectra of graphene grown on sapphire substrates in dependence of the plasma frequency (1–100 kHz). (h) Electro-optical characterization of directly grown few-layer graphene (FLG) via sheet resistance (circles) and UV-C transmittance (triangles) measurements. (i–k) Ni2p, Zn LLM, and O1s spectra confirming the successful growth of the NiO and ZnO thin films. (l) Transmittance spectra after each process step of graphene/NiO/ZnO heterojunction growth.

process, the defect-related D-peak is also observable with approx. $I_D/I_G \sim 1$, which originates from the high nucleation density, giving the graphene its typical nanocrystalline (nc) nature [36].

Interestingly, the Raman spectrum does not differ significantly when the plasma frequency is varied. To check, if this observation holds true for the electro-optical properties of these graphene films, electrical sheet resistance and optical absorption measurements were conducted and are shown in Figure 1h. The color scheme is kept constant as in the previous Figure 1g regarding the different frequencies from 1 to 100 kHz (blue to violet). The sheet resistance of the graphene films (left axis, spheres) shows a decrease from $R_S \sim 11.4$ kΩ/□ to $R_S \sim 3.6$ kΩ/□ when the frequency is increased from 1 to 100 kHz, respectively. The UV-C transmittance of the graphene films at a wavelength of 261 nm demonstrates a similar trend by decreasing from approx. 84% (1 kHz) to 71% (100 kHz). These trends can be explained by understanding the influence of the frequency of the pulsed DC plasma during PECVD graphene growth. The plasma frequency governs the rate of surface charge compensation. Consequently, lower frequencies likely impede growth by allowing charge build-up to repel positive CH_x species, whereas higher frequencies minimize this repulsion by frequently neutralizing the surface (Figure S2). The assumption that follows is that lower plasma frequencies produce thinner graphene layers with similar quality, as evidenced by the Raman signatures for otherwise constant growth parameters. This is exactly what is observed by the inverse relationship between sheet resistance and transmittance for nc-graphene, where thin layers are more transparent but also more electrically resistive [30]. Since an optimum between high transparency and low sheet resistance is desired, a plasma frequency of $f \sim 10$ kHz is chosen for further processing of the photodetectors.

Following the direct growth of graphene, the NiO/ZnO metal oxide heterostructure was sputtered on top (see Figure 1b). As a first step, the graphene-capped sapphire substrates are selectively covered with shadow masks, and a NiO thin film is sputtered in an

21951071, 0, Downloaded from https://advanced.onlinelibrary.wiley.com/doi/10.1002/adom.71412 by Universitaet Duisburg-Essen, Wiley Online Library on [02/07/2026]. See the Terms and Conditions (https://onlinelibrary.wiley.com/terms-and-conditions) on Wiley Online Library for rules of use; OA articles are governed by the applicable Creative Commons License

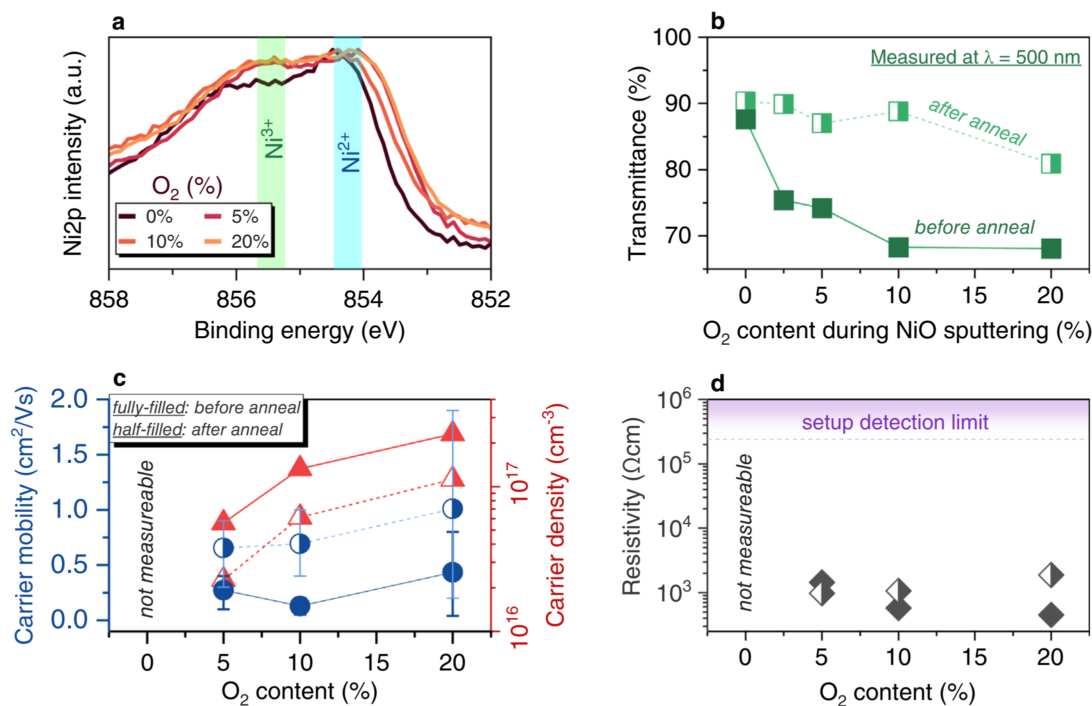

FIGURE 2 | Tuning NiO p-doping via oxygen-rich sputtering (0%–20% O_2) and post-annealing (60 min at 200°C in air). (a) XPS spectra revealing the emergence of Ni^{3+} states, indicative of *p*-type doping [31]. (b) Transmittance spectra showing that higher Ni^{3+} abundance increases absorption, while annealing partially restores transparency, which is beneficial for visible-blindness. (c) Hole concentration (red) and mobility (blue) versus O_2 content. Annealing slightly reduces carrier density but significantly increases mobility due to defect healing. (d) Resistivity versus O_2 content. Film resistance drops by at least two orders of magnitude upon O_2 introduction, confirming the critical role of oxygen in establishing p-conductivity.

atmosphere of argon and oxygen gas at pressures around 4 mbar. Due to NiO acting as the window layer (first UV-C sensitive layer in the pn-heterojunction) and an absorption coefficient of $\alpha \sim 5 \cdot 10^5$ cm^{-1} [37], its film thickness was chosen to be ~30 nm, thinner than typical literature values (>100 nm) [21, 22, 38]. The successful growth of NiO is proven by the Ni2p spectrum measured via x-ray photoelectron spectroscopy (XPS) as shown in Figure 1i. The doublet feature at binding energies ~855 eV originates from the different oxidation states of the Ni ions (Ni^{2+} and Ni^{3+}) in the NiO lattice. The satellite peaks at higher binding energies ~861 to 867 eV are a clear indicator for the formation of a metal oxide, in contrast to purely metallic Ni thin films. Figure 1j shows the O1s XPS spectrum of NiO (green) and compares the amount of lattice O vs. defective O, the latter most likely stemming from metal hydroxide layers like $Ni(OH)_2$ forming naturally on top of the sputtered NiO thin films [39].

The Gr/NiO samples are annealed at 200°C for 60 min in air (for a detailed discussion, see Figure 2), before a ZnO thin film is sputtered on top to form the metal oxide-based pn-heterojunction. Figure 1k shows the Zn LLM Auger transitions measured via XPS for 20 nm ZnO thin films, since the Zn2p spectrum essentially cannot differentiate well between the peaks for Zn vs. ZnO (Figure S4). Due to Auger transitions being a 3-electron process, the difference between highly conductive Zn and semiconducting ZnO is emphasized. For metallic Zn, leftover holes in the Zn lattice are rapidly screened due to an abundance of electrons refilling the empty states, resulting in higher kinetic energies of the Auger electrons (~991.5 eV). In the ZnO, however, this screening of positive charge is much slower due to all electrons being bound in the metal oxide lattice, which effectively leads to lower Auger electron kinetic energies ~988.1 eV. The O1s spectrum is another important measure to verify the quality of ZnO (s. Figure 1j), as most of the oxygen atoms are supposed to be bound in the lattice at lower binding energies (~ 529.9 eV). The higher binding energy peak at ~531.6 eV is related to defective O atoms and can be a direct marker for O-vacancies (V_O) induced n-doping in ZnO. The combination of Zn2p, Zn LLM, and O 1s spectra thus verifies high-quality sputtered ZnO thin films [40, 41].

As discussed above, the visible-blindness of the UV-C PDs is important to minimize visible-light-induced noise, e.g. for indoor UV-C applications. Figure 1l shows the optical transmittance spectra of the devices after each processing step. The dark-gray spectrum demonstrates the transmittance after FLG is grown directly onto the sapphire substrates. In the visible spectrum between 450 and 600 nm, T_{opt} ranges between 85% and 90%. After sputtering of 20 nm NiO and annealing the Gr/NiO stack, an absorption edge in the UV–vis spectrum with an optical bandgap of $E_{g,NiO} \sim 3.7$ eV is observed whereas the visible transmittance decreases to 76%–82%. This loss of visible transmittance originates from nickel vacancies V_{Ni} in NiO, which introduce in-gap defect states and will be further discussed below [42]. Subsequent sputtering of 20 nm ZnO introduces a second optical gap of $E_{g,ZnO} \sim 3.4$ eV. At the same time, the transmittance of the completed Gr/NiO/ZnO stack in the visible spectral range does not change, indicating that ZnO is fully transparent here.

21951071, 0, Downloaded from https://advanced.onlinelibrary.wiley.com/doi/10.1002/adom.71412 by Universitaet Duisburg-Essen, Wiley Online Library on [02/07/2026]. See the Terms and Conditions (https://onlinelibrary.wiley.com/terms-and-conditions) on Wiley Online Library for rules of use; OA articles are governed by the applicable Creative Commons License

To ensure p-doping of NiO required for forming a NiO/ZnO pn junction, either extrinsic or intrinsic doping mechanisms can be employed. The most common extrinsic acceptors constitute of Li^{1+} or Ag^{1+} cations, which substitute into vacant Ni^{2+} sites [31]. On the other hand, Ni^{2+} vacancies are the source of an intrinsic p-doping mechanism and can be easily controlled by the oxygen content during the sputtering process [31]. This is why in this work the stoichiometry of the sputtered NiO films was tuned by varying the oxygen flow ratio from 0% to 20% in an argon atmosphere. Investigating the structural evolution via atomic force probe microscopy revealed smoother NiO surfaces when the O-content during sputtering was increased (Figure S5).

XPS analysis reveals the chemical evolution of the films (Figure 2a). The Ni 2p spectrum is normalized to the lower binding energy feature around 854 – 855 eV, which resembles the lattice-bound Ni^{2+} ions. The introduction of oxygen during sputtering leads to the formation of nickel vacancies V_{Ni}, which introduce a charge imbalance into the NiO lattice [31]. This imbalance is compensated by the creation of Ni^{3+} ions, acting as localized hole states through which the carriers can traverse via a hopping mechanism [31]. The signature of these Ni^{3+} states is seen in spectral features around 855 – 856 eV, which emerge when oxygen is introduced during sputtering. Recent density functional theory calculations revealed that the emergence of Ni^{3+} hints toward the formation of non-stoichiometric NiO instead of an oxygen-rich, macroscopic Ni_2O_3 phase, the latter being highly unstable under standard sputtering conditions [43]. Interestingly, when the O_2 content is increased to 5, 10, and even 20%, no significant variance of the Ni^{3+} feature is observed. A potential explanation could originate in the surface-sensitive nature of the XPS analysis. In comparison to bulk, the amount of creatable acceptor states on the NiO surface is much lower and hence may saturate quite fast for minimal amounts of oxygen added during sputtering (here ~5%).

However, this increase of Ni^{3+}-based p-doping introduces an optical trade-off. As shown in Figure 2b, films with higher oxygen content exhibit reduced optical transmittance in the visible regime. For example, at 500 nm, a decrease from 88% to 68% transmittance is obtained when adding 10% of O_2. This "darkening" originates from the Ni vacancies, $V_{Ni,}$ which trap electrons from adjacent Ni^{2+}. To compensate for the missing positive charge, these adjacent Ni^{2+} cations oxidize to Ni^{3+}. The transformation to Ni^{3+}, however, also induces structural and electronic distortions within the lattice, leading to a stronger hybridization between the Ni 3d and O 2p orbitals [44]. It is this enhanced hybridization that generates localized in-gap defect-states and hence additional absorption pathways in the visible spectral region [42].

Post-deposition annealing (200°C for 60 min in air) is found to play a critical role in balancing this trade-off, as it partially restores the optical transparency and thereby improves the visible-blind rejection ratio of the final device. According to Li et al., this is caused by a recrystallization and reduction of lattice defects such as V_{Ni} and excess interstitial oxygen atoms that were incorporated during the O_2-rich sputtering process [45].

Hall effect measurements were performed to investigate the electrical charge transport and to quantify carrier mobility and carrier density, as well as to identify the carrier type of NiO in order to confirm its distinct p-type character. The main results are summarized in Figure 2c. The intrinsically low carrier mobility of NiO prepared without adding O_2 during the sputtering process precluded a reliable determination of the carrier type by Hall measurements. However, increasing the oxygen content during sputtering leads to an increase in hole carrier concentration up to 2×10^{17} cm^{-3} in case of the as-grown sample, confirming the effective generation of acceptor states. While the subsequent annealing step causes a slight reduction in carrier concentration—consistent with the recovery of optical transparency -, it yields a substantial benefit in carrier mobility, which almost triples and reaches values up to 1 cm^2/Vs . This mobility enhancement is attributed to the healing of lattice defects and the reduction of grain boundary scattering, which facilitates more efficient hole transport. Ultimately, the resistivity (Figure 2d) demonstrates that the presence of reactive oxygen during sputtering is the dominant factor for the electrical performance, since the transition from pure Ar sputtering to oxygen-rich sputtering is critical for getting measurable resistivities at all. While undoped NiO is above the setup detection limit ($\sim M\Omega$cm), the p-doped NiO thin films show significantly reduced resistivities in the order of $0.5 - 1.9\ k\Omega$cm, establishing the necessary conductivity of the p-channel required for self-powered operation [46].

Building on this optimized p-NiO, the device was finalized by processing the cathode by evaporating 200 nm of Al as UV-C reflective mirror (s. Methods), resulting in the completed device displayed in Figure 3a. The optical micrograph shows the top-view of a fully processed UV-C PD with the dark background representing the FLG film on sapphire (white arrow), which is contacted by the Ti/Au bottom electrode ring. The violet arrow indicates the sputtered p-NiO/n-ZnO layers with a diameter of 0.25 cm, which defines the active area of the PD (~ 0.05 cm^2). At the top, the device architecture is finalized by the Al electrode contacting the ZnO layer. The Al electrode serves as an ohmic contact to ZnO, acting as well as an UV-C mirror during the backside illumination of the PD [47].

Figure 3b shows the schematic band energy diagram of the PD architecture. The work function of graphene (~ 4.75 eV) was measured via Kelvin Probe Force microscopy (Figure S6), and the depicted electron affinities of the metal oxides, as well as the Al work function, are typical values agreed in literature [48]. By subtracting the experimentally observed optical bandgaps (Figure 1j), the valence band energies are estimated. The work function difference at the graphene/NiO (4.75 eV/5.2 eV [49]) interface suggests the formation of a slight contact potential barrier of 0.45 eV, which depends on the doping level of both materials [50]. However, previous studies have shown that doped metal oxide thin films on top of graphene are able to shift their Fermi level via charge transfer processes [51, 52]. Upon contact, electrons are assumed to spontaneously flow from the graphene into the NiO to equilibrate the Fermi levels. Because graphene has a low density of states, this electron depletion heavily p-dopes the graphene, shifting its Fermi level significantly downward [52]. This charge transfer is reported to create a strong interfacial dipole that virtually aligns the effective work function of the graphene with the valence band of the NiO [52]. Thus, the initial potential barrier is reduced, facilitating highly efficient,

21951071, 0, Downloaded from https://advanced.onlinelibrary.wiley.com/doi/10.1002/adom.71412 by Universitaet Duisburg-Essen, Wiley Online Library on [02/07/2026]. See the Terms and Conditions (https://onlinelibrary.wiley.com/terms-and-conditions) on Wiley Online Library for rules of use; OA articles are governed by the applicable Creative Commons License

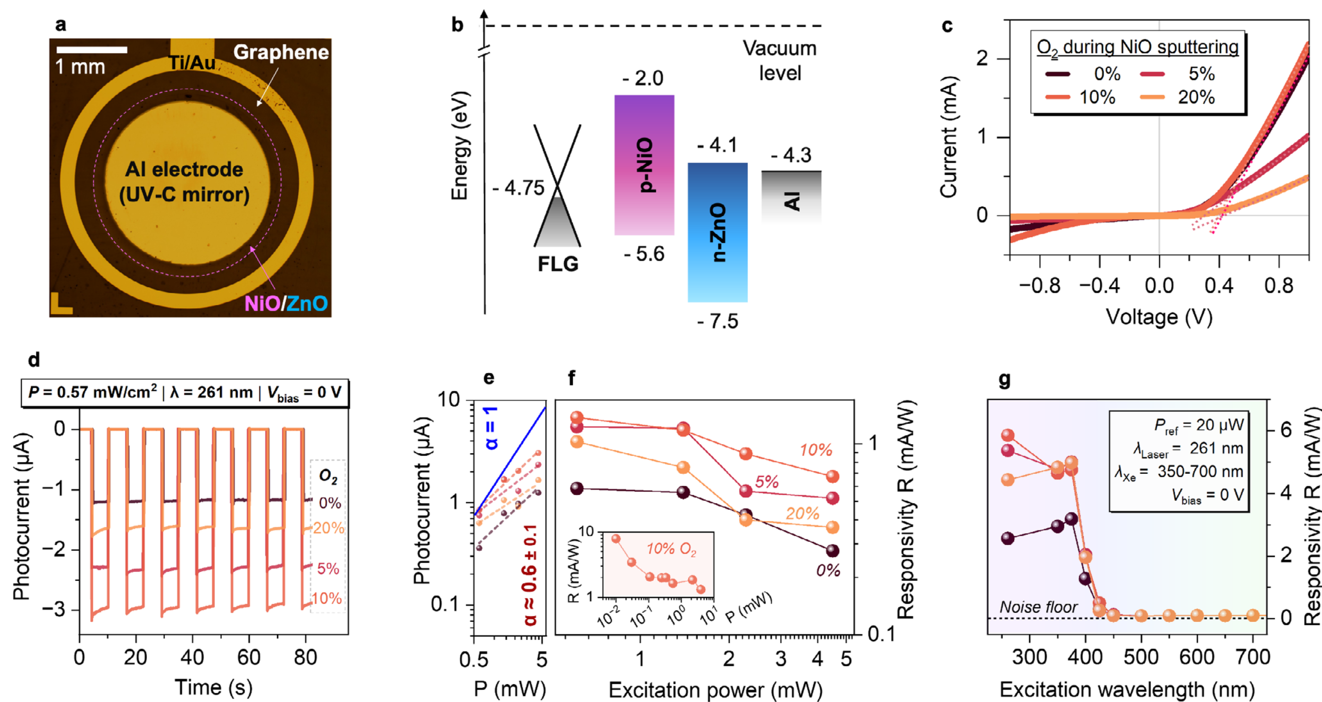

FIGURE 3 | UV-C photodiode characterization. (a) Optical micrograph of finalized PD. (b) Schematic band diagram showing the NiO/ZnO type-II heterojunction with graphene and Al electrodes contacting the metal oxides. (c) Current-voltage plots showing a diode-like rectifying behavior for UV-C PDs with different O_2-flow during p-NiO deposition. (d) Transient photoresponse of the UV-C PDs over a time span of 90 s for modulated light exposure. (e) Photocurrent and (f) responsivity of the detectors in dependence of excitation power in log-log scales, demonstrating sub-linear photoresponse. (g) Spectral photoresponse of the detectors showcasing excellent visible-blindness.

quasi-ohmic transport of photogenerated holes from the NiO into the graphene anode [50, 53].

The separation of photogenerated charge carriers is mostly governed by the heterojunction interface between NiO/ZnO, specifically by the type-II transition and the built-in field that arises upon contact of these *p*- and *n*-type materials. The type-II band alignment arises from the conduction band minimum and valence band maximum of the p-NiO being positioned higher than the corresponding bands in the n-ZnO. When photons are absorbed and converted to electron-hole pairs at the pn-junction, this type-II alignment, coupled with the strong built-in electric field of the depletion region in the pn-junction, facilitates the separation of the charge carriers, with the electrons being swept toward the n-side (ZnO) and the holes driven toward the p-side (NiO). The potential of the built-in field depends on the electron affinities and doping levels of the metal oxides and can range between 0.4 and 2.3 V (s. Methods). To experimentally validate the operation of the pn-junction, we analyze the current-voltage characteristics of the fully assembled UV-C PDs for different O_2-percentages (0%, 5%, 10%, and 20%) that were used during the NiO sputtering (see Figure 3c). For all devices, diode-like rectifying behaviors are observed. In the forward bias regime, a turn-on voltage of 0.3 – 0.4 V is observed. Notably, these turn-voltages are at the lower end of the calculated range between 0.4 and 2.3 V. This, however, is an expected behavior due to the defect-prone nature of non-epitaxially grown metal oxide interfaces. In the literature, a vast variety of turn-on voltages V_{bi} higher than 1.2 V are reported, mainly due variations in processing techniques, materials quality, and characterization methods [22, 23, 54–58].

The transient photoresponse after pulsed excitation serves as a fundamental benchmark for the performance of self-powered photodetectors, rigorously evaluating both the signal contrast between the illuminated (ON) and dark (OFF) states and the switching speed between them. Figure 3d demonstrates the transient photoresponse for devices with different NiO p-doping (same color scheme as Figure 3c) measured in self-powered mode (zero bias). Once the detector is illuminated with a wavelength of 261 nm and a power density of approximately 0.57 mW/cm^2, photocurrents up to 3 µA are observed. Considering the finite dark current of ~250 pA that may originate from thermally activated interface defect states at the sputtered NiO/ZnO heterojunction [56], a photoresponse with an excellent ON-OFF ratio > 10^4 is obtained. All detectors show high switching speeds between ON/OFF states faster than 50 ms, which represents the data collection speed limit of our setup (Figure S7).

With increasing O_2-content from 0% to 10% O_2, an increase in photocurrent is observed from 1.2 to 3 µA. This enhancement can be attributed to the progressive p-doping of the NiO layer, which is essential for establishing a robust pn junction. As the hole concentration rises, the Fermi level shifts toward the valence band, thereby increasing the built-in potential V_{bi} at the NiO/ZnO interface. This stronger internal field is critical for the efficient separation of charge carriers in self-powered operation. A further increase to 20% O_2 however, leads to a decrease in photocurrent to ~1.6 µA, identifying 10% O_2 as the optimal condition. This drop in photocurrent is likely driven by changes in the NiO material properties following the thermal annealing step required for device fabrication. While the as-deposited NiO films become

21951071, 0, Downloaded from https://advanced.onlinelibrary.wiley.com/doi/10.1002/adom.71412 by Universitaet Duisburg-Essen, Wiley Online Library on [02/07/2026]. See the Terms and Conditions (https://onlinelibrary.wiley.com/terms-and-conditions) on Wiley Online Library for rules of use; OA articles are governed by the applicable Creative Commons License

more conductive with oxygen, the macroscopic resistivity of the 20% film increases significantly after annealing, introducing resistive losses that could hinder photogenerated charge carrier extraction (Figure 2d).

A further performance parameter is the linear dynamic range of a photodetector. In theory, the photocurrent I_{ph} scales with the excitation power P with $\propto P^{\alpha}$ [59], where α is the power-law exponent describing the functioning principle of the photodetector. Hereby, $\alpha = 1$ would indicate a linear photoresponse usually seen in PDs with power-independent carrier lifetimes and band-to-band recombination. Figure 3e depicts I_{ph} vs. P for the different devices in a log-log plot. The solid blue line indicates $\alpha = 1$. Averaging over all devices, a value of $\alpha = 0.6 \pm 0.1$ is extracted, indicating a similar sub-linear photoresponse for all levels of NiO p-doping [59]. Contradictory to a typical Si-based PD, a sublinear photoresponse is very much expected for the sputtered metal oxide heterojunction studied in this work [60, 61]. On the one hand, sputtering offers easily controllable introduction of "desired defects" into the metal oxide lattices such as V_O in ZnO (n-dopant) [62] and V_{Ni} in Ni (p-dopant) [20]. On the other hand, sputtering is known to yield higher amounts of surface and interface defects, leading to energetically deep trap states [60]. Importantly, these trapping processes are exaggerated at low powers, since most trap states are still unoccupied. When the power is increased substantially, most of the trap states are getting occupied, which leads to an increase of the recombination rate at high power and hence lower photoresponse, resulting in a sub-linear relation between photocurrent and excitation power. As one of the most important figures of merit, the responsivities of all detectors are summarized in Figure 3f. Consistent to previous observations, the 10% O_2 sample shows the highest responsivities. According to the photodetection mechanism described before, a maximum responsivity should be observed at the lowest possible excitation power. This is shown in the inset of Figure 3f for the best performing device (10% O_2) where a maximum responsivity of $R \approx 7.9$ mA/W is demonstrated at a minimum power density of $P \approx 10\ \mu\text{W/cm}^2$.

As discussed before, the visible-blindness of the photodetector is important to minimize interference from visible light, for example, during UV-C monitoring in germicidal applications. To study the spectral response of the PDs, illumination wavelength-dependent photoresponse measurements are conducted and shown in Figure 3f for a reference excitation power of $P_{ref} \approx 20\ \mu$W (s. Methods section). For this, UV-C and UV-B-to-vis excitations are achieved by a 261 nm laser and an Xe-lamp with a monochromator selecting the desired wavelength, respectively. The noise level of the Xe-lamp and hence the minimally resolvable responsivity of ~13 µA/W (depicted as the dashed line) is derived from the dark current (~254 pA) using $P_{ref} \approx 20\ \mu$W. The wavelength dependent responsivities are plotted in Figure 3g for different O_2-percentage during NiO sputtering. The most significant differences are observed between devices with undoped (0%) vs. p-doped (5, 10, 20% O_2) NiO films where responsivities in the UV-regime are almost doubled when any amount of O_2-induced p-doping is present. Between the different UV-bands, no significant spectral dependence is seen, with responsivities ranging between 5 and 6 mA/W. For wavelengths between 375 and 425 nm, a drop in responsivity down to ~ 0.5 mA/W occurs for all devices. This observed photoresponse can be attributed to a residual absorption caused by the Urbach tails of the metal oxides [63], which are typically observed in low-temperature sputtered thin films. Moving further into the visible range, the measured photoresponse (e.g. ~ 15 µA/W at 500 nm) reaches the experimental noise floor of approximately ~ 13 µA/W. This demonstrates a lack of charge carrier generation under visible illumination. This observation validates the expectations since the energies of "visible" photons fall below the nominal optical bandgaps of both NiO (~3.7 eV) and ZnO (~3.4 eV), meaning that the incident radiation becomes insufficient to drive direct electron transitions from the valence to the conduction band. Consequently, bulk charge carrier photogeneration is effectively suppressed, yielding a UV-to-visible rejection ratio of more than two orders of magnitude and experimentally confirming the device's excellent intrinsic visible-blindness.

3 | Discussion

The development of high-performance UV-C optoelectronics is often hindered by the limitations of conventional transparent conducting oxides (TCOs) like Indium Tin Oxide (ITO), which becomes opaque for wavelengths below 350 nm.

In this work, we address these gaps by integrating graphene electrodes with defect-engineered metal oxides that form a pn junction on a UV-C transparent sapphire substrate. This architecture utilizes the broad spectral transparency of CVD graphene for transmitting UV-C light while acting as an electrode, the built-in field of the metal oxide pn-junction to drive current even at zero-bias, and a back-side Aluminum (Al) mirror to maximize photon path length within the active layer, providing a path toward high-efficiency, low-cost fabrication.

A key factor in this architecture is the favorable charge transport observed between the graphene anode and the p-NiO layer. While a significant potential barrier might be expected given their work function difference, exceptionally high photocurrents up to 3 µA without any applied bias (self-powered operation) hint toward the formation of quasi-ohmic contacts due to interface dipoles that facilitate hole transport through charge transfer doping processes known from literature. This alignment allows the CVD-grown graphene to function as an effective hole-collection electrode, overcoming the spectral cut-off of conventional ITO for wavelengths < 350 nm and extending device operation into the deep-UV-C window without sacrificing carrier collection efficiency.

Crucially, the performance of the final detector relies on the stoichiometric tuning of the p-NiO layer. Our results highlight a fundamental balance: excess oxygen while sputtering is necessary to generate nickel vacancies acting as acceptors, yielding a p-doping level up to $p \sim 2 \times 10^{17}\text{cm}^{-3}$, yet it simultaneously introduces sub-bandgap states that can reduce optical transmission. We find that post-deposition annealing acts as a critical optimization step, selectively reducing structural disorder to restore the optical band edge while preserving sufficient vacancy acceptors for *p*-type conductivity. This engineering allows the device to maintain a built-in potential capable of driving zero-bias operation, which is essential for energy-autonomous sensing. The device's spectral selectivity arises directly from the wide bandgaps

21951071, 0, Downloaded from https://advanced.onlinelibrary.wiley.com/doi/10.1002/adom.71412 by Universitaet Duisburg-Essen, Wiley Online Library on [02/07/2026]. See the Terms and Conditions (https://onlinelibrary.wiley.com/terms-and-conditions) on Wiley Online Library for rules of use; OA articles are governed by the applicable Creative Commons License

of the constituent oxides, effectively rejecting visible light without the need for external filters. The devices exhibit rapid temporal switching, suggesting that carrier extraction is efficient enough to support dynamic monitoring applications.

When contextualizing this performance against traditional silicon-based technologies, the unique advantages of our architecture become apparent. While highly optimized Si-based photodetectors can achieve exceptional responsivities of ~200 mA/W in the UV-C regime, their narrow bandgap inherently requires complex device geometries and the integration of bulky external optical filters to block ambient light in the visible spectral range. In contrast, our device architecture enables intrinsic visible-blindness due to the wide-bandgaps of the metal oxides. At the same time, the thin film deposition itself, as well as the p/n-doping processes, are done in highly scalable, low-cost sputtering processes.

Ultimately, this all-oxide approach demonstrates the potential of combining industrial magnetron sputtering with direct CVD growth on standard sapphire substrates. By bridging the processing of 2D materials with bulk metal oxides, this work establishes a scalable platform for transparent, self-powered UV-C photodetection devices. The true impact of this architecture lies in its potential for wafer-scale integration to meet the rising global demand for solar-blind technologies. Applications such as autonomous dosage monitoring in water purification and secure optical communications require exactly these types of highly sensitive, energy-independent sensor nodes. Furthermore, because our fabrication avoids the prohibitive costs and lattice-mismatch issues of traditional deep-UV epitaxy, it provides a direct, cost-effective pathway toward high-resolution UV-C imaging arrays. To transition from single-pixel devices to commercial arrays, future research must address large-area uniformity at the graphene-oxide interface and integration with standard readout circuitry. Additionally, enhancing the UV-to-visible rejection ratio will require tailoring the NiO/ZnO heterostructure to suppress sub-bandgap absorption while maintaining a high-quality p-n junction. This could be achieved, e.g., by transitioning from intrinsic defect engineering to the introduction of external dopants (e.g., Li^+ or Ag^+), which mitigate the formation of visible-absorbing mid-gap states. Overcoming these hurdles will pave the way for a new generation of low-cost, energy-autonomous deep-UV optoelectronics.

4 | Materials and Methods

4.1 | Sapphire Wafer Preparation

C-plane sapphire wafers from the company *Helios New Materials Ltd. (Jiangyin, Jiangsu, CN)* with a thickness of 430 µm (and initial 2-inch diameter) were cut into 1 × 1 cm^2 pieces and used as graphene growth substrates. Before insertion into the PECVD reactor chamber, the sapphire substrates were cleaned in a boiling acetone bath for 3 min. Afterward, ultra-sonication followed for 2 min, and the solvent-bath/sonication process was repeated for ethanol. with a consecutive ultra-sonication for 2 min. Lastly, the substrates were rinsed with isopropanol and blow-dried under nitrogen gas.

4.2 | Graphene Growth via Plasma-Enhanced Chemical Vapor Deposition

Graphene was synthesized in a 4-inch cold-wall PECVD system (Black Magic) from *AIXTRON SE (Herzogenrath, DE)*. The reactor configuration includes a resistively heated graphite heater and a graphite susceptor positioned above it, serving as the sample holder. A second graphite element, functioning both as a (top) heater and counter electrode, is installed approximately 10 cm above the lower electrode. An exterior and interior view of the system and the reactor chamber, including these components, is provided in Figure S1. Temperature monitoring is performed using two thermocouples. One sensor is embedded in the top heater, while the second is placed onto a dummy substrate close to the actual sample position. This latter sensor, referred to as the surface thermocouple (SFTC), is shielded by a quartz tube to prevent plasma-induced degradation. All temperatures reported throughout this study correspond to the readings obtained from the SFTC.

Methane (CH_4), nitrogen (N_2), and argon (Ar) were employed as precursor and carrier gases. The process begins with heating the reactor to the target temperature at a ramp rate of 150°C min^{-1} under 800 sccm N_2 at a chamber pressure of 10 mbar. Upon reaching the growth temperature, the nitrogen flow is reduced to 200 and 5 sccm CH_4 is introduced. Subsequently, a capacitively coupled DC plasma is ignited between the lower graphite electrode and the upper graphite heater, which simultaneously acts as the counter electrode. Plasma excitation is operated in pulsed mode, with frequencies varied between 1 and 100 kHz (see Figure S2). During each pulse cycle, a short polarity reversal lasting 1–10 µs is implemented to neutralize charge accumulation on the dielectric sapphire substrates. The bias voltage depends on the plasma power, which was maintained at 50 W for all experiments. Growth was conducted at a substrate temperature of 670°C (SFTC reading) for a fixed duration of 30 min. Additional technical details of the reactor design are available elsewhere [30]. After completion of the deposition step, active heating is discontinued, and the system is allowed to cool naturally under a high flow of inert gas (2000 sccm Ar and 500 sccm N_2). The cooldown period lasts approximately 40 min, reaching ~200°C before sample removal. A schematic overview of the full growth sequence is shown in Figure S1.

4.3 | Sputtering of Metal Oxides and Device Fabrication

To deposit pn-heterojunction consisting of NiO and ZnO onto the sapphire/graphene template, a customized *ECOvap* RF-sputtering system from the company *MBRAUN (Garching, DE)* is used. For NiO sputtering, a gas flow mixture of Ar/O_2 is used, whereas the O_2 flow was varied between 0% and 20%. At the same time, the total gas flow rate was kept at 50 sccm, meaning that an O_2 percentage of 10% was achieved by using a gas flow mixture of 45/5 sccm of Ar/O_2. The thickness of NiO was varied between 20 and 100 nm, depending on the characterization method, with deposition rates of approximately 1 nm/min. For the XPS and transmittance measurements presented in Figure 1, both NiO and ZnO thin films were 20 nm thick. For Hall measurements, 100 nm thick NiO layers were used to ensure

21951071, 0, Downloaded from https://advanced.onlinelibrary.wiley.com/doi/10.1002/adom.71412 by Universitaet Duisburg-Essen, Wiley Online Library on [02/07/2026]. See the Terms and Conditions (https://onlinelibrary.wiley.com/terms-and-conditions) on Wiley Online Library for rules of use; OA articles are governed by the applicable Creative Commons License

sufficient conductivity since NiO is known for its low charge carrier mobility.

In the final detectors, 30 nm of NiO were deposited to ensure sufficient photons reach the pn-junction at the NiO/ZnO interface. The chamber pressure during NiO sputtering was approx. 4 mbar. During the deposition process, the sample holder on which the substrate was attached was rotating to ensure homogenous growth of NiO. After the deposition, the NiO thin films were annealed at 200°C for 60 min on a hotplate in air for some of the experiments. After this, the samples were then loaded back into the sputter chamber, and ZnO was sputtered with approx 60 nm to form the metal oxide pn-heterojunction. Here, a gas flow consisting only of 50 sccm argon was used, and the chamber pressure was at ~ 4 mbar. The deposition rate was kept between 1.5 and 2 nm/min. Finally, the ring-shaped bottom contacts with an inner diameter of 3.0 mm were processed via optical lithography using AZ nLOF 2070 negative photoresist, developed in AZ 326 MIF following standard spin-coating, baking (110°C), and UV exposure steps. A Ti/Au (15/85 nm) metal stack was subsequently deposited by employing electron-beam evaporation for the Ti adhesion layer and thermal evaporation for the Au -followed by a standard lift-off process. Lastly, a 200 nm thick Aluminum (Al) top contact was electron-beam evaporated. To prevent electrical short-circuiting between the electrodes, the Al contact was defined using a smaller shadow mask (2.5 mm in diameter) in comparison to the metal oxide stack, most importantly confining it within the oxide area.

4.4 | Characterization Methods

The directly grown graphene layers were characterized with Raman spectroscopy. For this, a confocal NTEGRA Spectra system from *NT-MDT BV (Apeldoorn, NL)* is used. The spectra were measured combining an excitation wavelength of 532 nm, a laser spot size < 0.5 µm, a spectral resolution < 4 cm^{-1}, a pinhole of 50 µm, and an integration time of 10 s. The Raman spectra were measured in the center of the square-shaped samples and averaged over three single measurements. A UV–vis Spectrophotometer UV-2550 from *Shimadzu Corp. (Kyoto, JP)* is used to obtain transmittance spectra in the spectral range of 300–800 nm. All transmittance measurements were compared to graphene-free reference c-plane sapphire substrates. Topography and contact potential difference information of the grown graphene layers on sapphire were obtained via a *Bruker Corp. (Billerica, MA, USA)* Innova AFM system in combination with a *Zurich Instruments AG (Zürich, CH)* MFLI lock-in amplifier and PID controller, used for the extraction of a Kelvin signal. Surface-sensitive x-ray and ultraviolet photoelectron spectroscopy measurements were performed with a PHI 5000 VersaProbe II from *Physical Electronics GmbH (Feldkirchen, DE)*.

Sheet resistance measurements were conducted using a four-point probe system with a probe spacing of 1.27 mm from *Ossila Ltd. (Sheffield, GB)*. By averaging over four measurements, where the sample was rotated by 90° consequently, the influence of possible inhomogeneities of the directly grown graphene layer were mitigated. Hall effect measurements in van der Pauw geometry were carried out to determine the carrier density and mobility of NiO with 100 nm thickness. Ni/Au (5 nm /110 nm) contacts were deposited at the sample corners and exhibited ohmic behavior. Measurements were conducted at room temperature under vacuum. A constant current was applied using a *Keithley* 2400 source meter, and the (Hall) voltage was measured using a *Keithley* 2000 Digital Multimeter. A perpendicular magnetic field of up to 1.2 T was applied using a *Bruker* B-E 10 electromagnet. Hall voltage measurements were recorded using two cross-configurations with current reversal of each combination of the Van der Pauw geometry. During the measurements, the magnetic field was ramped gradually from 0 to +1.2 T, then decreased to −1.2 T, and finally returned to 0 T. To obtain the optimal average Hall voltage, all individual traces were symmetrized and aligned to a consistent polarity (i.e., normalized in direction) before averaging and calculating standard deviation. The schematic of the measurement setup and the equations used for the analysis can be found in previous publications [64].

UV-C photoresponse measurements of the final PDs were carried out using a 261 nm solid-state laser by *HT-Laser UG (Münster, DE)*. The laser beam was expanded by a simple two-lens setup to uniformly illuminate the whole active area ~ 0.05 cm^2 of the PDs. A powermeter was used to determine the power densities arriving at the active area. For spectral photoresponse measurements, a 75 W Xe-lamp (LSB511) from *Quantum Design GmbH (Pfungstadt, DE)* was used in combination with a "*Omni-λ200*" monochromator from *Zolix Instruments Co., Ltd. (Beijing, CN)*. The resulting power densities arriving at the active area of the PDs were measured with powermeters. All photoresponse measurements were taken by contacting the devices with two probing tips on the p- (Ti/Au contact) and the n-side (Al contact) and using a *Keysight* B2901BL to measure the dark- and photocurrents of the devices.

4.5 | Calculation of Built-in Potential at NiO/ZnO pn-Junction

The built-in potential V_{bi} of the NiO/ZnO heterojunction was calculated analytically to determine the range of possible values resulting from the spread of electron affinities reported in the literature. V_{bi} was determined using the relation [65]:

$$q\,V_{bi} = \left(\chi_{p-NiO} - \chi_{n-ZnO}\right) + E_{g,NiO} - \delta_{p-NiO} - \delta_{n-ZnO}$$

where χ_{p-NiO} represents the electron affinity and $E_{g,NiO}$ the bandgap of NiO. The terms $\delta_{p-NiO} = E_F - E_{VBM}$ and $\delta_{n-ZnO} = E_F - E_{CBM}$ denote the positions of the Fermi level relative to the respective band edges. Using a hole concentration of $p = 1.12 \cdot 10^{17} cm^{-3}$ from Figure 2c, δ_{p-NiO} was calculated to be 0.12 eV. For ZnO, an electron concentration of $n = 1 \cdot 10^{19} cm^{-3}$ was approximated for sputtered thin films from literature [62], which results in a degenerate condition where the Fermi level lies approximately 0.09 eV above the conduction band minimum (yielding a value of $\delta_{n-ZnO} = -0.09$ eV). Applying the fixed bandgaps ($E_{g,NiO} = 3.6$ eV, $E_{g,ZnO} = 3.4$ eV) and varying the electron affinities from literature ($\chi_{p-NiO} = 1.46 - 2.46$ eV; $\chi_{n-ZnO} = 3.7 - 4.6$ eV), we identified a theoretical V_{bi}-range from ~ 0.4 to 2.3 V.

21951071, 0, Downloaded from https://advanced.onlinelibrary.wiley.com/doi/10.1002/adom.71412 by Universitaet Duisburg-Essen, Wiley Online Library on [02/07/2026]. See the Terms and Conditions (https://onlinelibrary.wiley.com/terms-and-conditions) on Wiley Online Library for rules of use; OA articles are governed by the applicable Creative Commons License

4.6 | Spectral Responsivity Calculation

The spectral responsivity $R(\lambda)$ was determined by measuring the device photocurrent under monochromatic excitation from a Xenon arc lamp (250–700 nm). To account for the non-uniform spectral power distribution of the lamp and the sub-linear power response of the photodetector, a normalization procedure was applied. The detectors power-dependent responsivities were first characterized at a fixed wavelength in the UV-C regime via a 261 nm laser, revealing a power-law relationship with $\alpha \approx 0.56$. All measured spectral data were then normalized to a constant reference power of $P_{\mathrm{ref}} = 20\ \mu W$ using the correction relation:

$$R_{\mathrm{corr}}\ (\lambda) = R_{\mathrm{meas}}\ (\lambda) \cdot \left(\frac{P_{\mathrm{ref}}}{P_{\mathrm{meas}}}\right)^{\alpha-1}$$

This procedure effectively decoupled the spectral dependence from the power-induced non-linearity, ensuring an accurate representation of the detector's intrinsic spectral characteristics.

Author Contributions

U.K. fabricated the graphene samples and processed the photodetector devices, including the sputtering of metal oxide thin films and metallization via optical lithography. The U.K. also installed the photodetector characterization setups and performed photoresponse measurements. L.L. assisted in the processing chain and characterization of photodetector devices. U.K., W.M., and G.B. evaluated the results of the graphene growth and photodetector processing. Y.J. conducted Hall- and electrical measurements on the sputtered NiO thin films. Y.J. and A.L. evaluated the results of these electrical transport measurements. U.K. wrote the manuscript, which was further improved by Y.J., A.L., W.M and G.B. All authors reviewed the results and approved the final version of the manuscript.

Acknowledgements

This work was supported by the German Research Foundation (Deutsche Forschungsgemeinschaft, DFG) within the IRTG 2803 (Project No. 461605777). The authors acknowledge the Interdisciplinary Center for Analytics on the Nanoscale (ICAN) of the University of Duisburg-Essen, especially Dr. Ulrich Hagemann for conducting XPS and UPS measurements. The authors also thank Sofiia Ustenko for conducting KPFM measurements and Nico Schwarz for Hall measurements.

Open access funding enabled and organized by Projekt DEAL.

Conflicts of Interest

The authors declare no conflicts of interest.

Data Availability Statement

The data that support the findings of this study are openly available under the following DOI: https://doi.org/10.71955/DUEDATA-2026-MQFDHMMC.

References

1. B. T. Dewes, T. Klee, N. D. Cottam, et al., "Fast Ultraviolet-C Photonics: Generating and Sensing Laser Pulses on Femtosecond Timescales," *Light: Science & Applications* 14 (2025): 384, https://doi.org/10.1038/s41377-025-02042-2.

2. A. Vavoulas, H. G. Sandalidis, N. D. Chatzidiamantis, Z. Xu, and G. K. Karagiannidis, "A Survey on Ultraviolet C-Band (UV-C) Communications," *IEEE Communications Surveys & Tutorials* 21 (2019): 2111–2133, https://doi.org/10.1109/COMST.2019.2898946.

3. Z. Qi, L. Wang, Y. Liang, P. Liu, H. Zhu, and Y. Wang, "Deep-Ultraviolet Light Communication in Sunlight Using 275-nm LEDs," *Applied Physics Letters* 123 (2023): 161109, https://doi.org/10.1063/5.0169319.

4. T. M. H. Nguyen, S. G. Shin, H. W. Choi, and C. W. Bark, "Recent Advances in Self-Powered and Flexible UVC Photodetectors," *Exploration* 2 (2022): 20210078, https://doi.org/10.1002/EXP.20210078.

5. S. Liang and W. Sun, "Recent Advances in Packaging Technologies of AlGaN-Based Deep Ultraviolet Light-Emitting Diodes," *Advanced Materials Technologies* 7 (2022): 2101502, https://doi.org/10.1002/admt.202101502.

6. M. Kneissl, T.-Y. Seong, J. Han, and H. Amano, "The Emergence and Prospects of Deep-Ultraviolet Light-Emitting Diode Technologies," *Nature Photonics* 13 (2019): 233–244, https://doi.org/10.1038/s41566-019-0359-9.

7. V. K. Sharma and H. V. Demir, "Bright Future of Deep-Ultraviolet Photonics: Emerging UVC Chip-Scale Light-Source Technology Platforms, Benchmarking, Challenges, and Outlook for UV Disinfection," *ACS Photonics* 9 (2022): 1513–1521, https://doi.org/10.1021/acsphotonics.2c00041.

8. F. Cao, Y. Liu, M. Liu, et al., "Wide Bandgap Semiconductors for Ultraviolet Photodetectors: Approaches, Applications, and Prospects," *Research* 7 (2024): 385, https://doi.org/10.34133/research.0385.

9. L. Sang, M. Liao, and M. Sumiya, "A Comprehensive Review of Semiconductor Ultraviolet Photodetectors: From Thin Film to One-Dimensional Nanostructures," *Sensors* 13 (2013): 10482–10518, https://doi.org/10.3390/s130810482.

10. M. F. Al Fattah, A. A. Khan, H. Anabestani, et al., "Sensing of Ultraviolet Light: A Transition From Conventional to Self-Powered Photodetector," *Nanoscale* 13 (2021): 15526–15551, https://doi.org/10.1039/d1nr04561j.

11. Y. Li, W. Zheng, and F. Huang, "All-silicon Photovoltaic Detectors With Deep Ultraviolet Selectivity," *PhotoniX* 1 (2020): 15, https://doi.org/10.1186/s43074-020-00014-w.

12. C. V. Prasad, P. Dharmaiah, G. H. Lee, et al., "Interface Engineering of 4H-SiC-Based UV photodetectors: A Comprehensive Review," *Materials Today Advances* 28 (2025): 100662, https://doi.org/10.1016/j.mtadv.2025.100662.

13. S. Nikishin, A. Bernussi, and S. Karpov, "Towards Efficient Electrically-Driven Deep UVC Lasing: Challenges and Opportunities," *Nanomaterials* 13 (2022): 185, https://doi.org/10.3390/nano13010185.

14. M. Becker, S. L. Benz, L. Chen, et al., "Controlled Thin-film Deposition of α or β Ga_2O_3 by Ion-beam sputtering," *Journal of Vacuum Science & Technology A: Vacuum, Surfaces, and Films* 38 (2020): 063412, https://doi.org/10.1116/6.0000619.

15. H. Singh, S. K. Bhardwaj, M. Khatri, K.-H. Kim, and N. Bhardwaj, "UVC Radiation for Food Safety: An Emerging Technology for the Microbial Disinfection of Food Products," *Chemical Engineering Journal* 417 (2021): 128084, https://doi.org/10.1016/j.cej.2020.128084.

16. F. Trier, D. V. Christensen, and N. Pryds, "Electron Mobility in Oxide Heterostructures," *Journal of Physics D: Applied Physics* 51 (2018): 293002, https://doi.org/10.1088/1361-6463/aac9aa.

17. L. Su, T. Li, and Y. Zhu, "A Vertical $CsPbBr_3$/ZnO Heterojunction for Photo-sensing Lights From UV to Green Band," *Optics Express* 30 (2022): 23330–23340, https://doi.org/10.1364/OE.463394.

18. L. Su, Y. Zhu, X. Xu, H. Chen, Z. Tang, and X. Fang, "Back-to-back Symmetric Schottky Type UVA Photodetector Based on Ternary Alloy BeZnO," *Journal of Materials Chemistry C* 6 (2018): 7776–7782, https://doi.org/10.1039/C8TC02255K.

19. Z. Wang, P. K. Nayak, J. A. Caraveo-Frescas, and H. N. Alshareef, "Recent Developments in p-Type Oxide Semiconductor Materials and

21951071, 0, Downloaded from https://advanced.onlinelibrary.wiley.com/doi/10.1002/adom.71412 by Universitaet Duisburg-Essen, Wiley Online Library on [02/07/2026]. See the Terms and Conditions (https://onlinelibrary.wiley.com/terms-and-conditions) on Wiley Online Library for rules of use; OA articles are governed by the applicable Creative Commons License

Devices," *Advanced Materials* 28 (2016): 3831–3892, https://doi.org/10.1002/adma.201503080.

20. Z. Y. Xu, C. P. Liu, X. S. Wang, et al., "A p-Type Wide Bandgap $Ni_xIn_{1-x}O_{1+\delta}$ Oxide Alloy With Enhanced Hole Mobility for High Rectifying p-n Heterojunction Diodes," *ACS Applied Materials & Interfaces* 18 (2026): 5443–5454, https://doi.org/10.1021/acsami.5c19042.

21. A. B. U. Rahman, S. Begum, N. M. S. Kaawash, et al., "p-NiO/n-ZnO Heterojunctions for Visible-Blind UV and IR Photodetectors: A Low-Temperature Fabrication Approach," *Physica B: Condensed Matter* 694 (2024): 416478, https://doi.org/10.1016/j.physb.2024.416478.

22. M. Jia, F. Wang, L. Tang, et al., "Low-Power-Consumption Ultraviolet Photodetector Based on p-NiO/SiO_2/n-ZnO," *Optics & Laser Technology* 157 (2023): 108634, https://doi.org/10.1016/j.optlastec.2022.108634.

23. G. Shang, L. Tang, G. Wu, et al., "High-Performance NiO/TiO_2/ZnO Photovoltaic UV Detector," *Sensors* 23 (2023): 2741, https://doi.org/10.3390/s23052741.

24. P. Li, H. Shi, K. Chen, et al., "Construction of GaN/Ga_2 O_3 p–n Junction for an Extremely High Responsivity Self-Powered UV Photodetector," *Journal of Materials Chemistry C* 5 (2017): 10562–10570, https://doi.org/10.1039/C7TC03746E.

25. M.-M. Fan, K.-L. Xu, X.-Y. Li, G.-H. He, and L. Cao, "Self-Powered Solar-Blind UV/Visible Dual-Band Photodetection Based on a Solid-state PEDOT:PSS/α-Ga_2 O_3 Nanorod Array/FTO Photodetector," *Journal of Materials Chemistry C* 9 (2021): 16459–16467, https://doi.org/10.1039/D1TC04091J.

26. Y. Wang, L. Li, H. Wang, et al., "An Ultrahigh Responsivity Self-Powered Solar-Blind Photodetector Based on a Centimeter-sized β-Ga_2O_3/Polyaniline Heterojunction," *Nanoscale* 12 (2020): 1406–1413, https://doi.org/10.1039/c9nr09095a.

27. X. Yang, J. Lin, S. Huang, et al., "Semiconductor Applications of Yb_2O_3: Constructing Heterojunction Solar-blind UV Photodetectors With Graphene," *Applied Physics Letters* 123 (2023): 081103, https://doi.org/10.1063/5.0163938.

28. T. M. H. Nguyen, S. K. Lee, S. Kim, and C. W. Bark, "Practical Demonstration of Deep-Ultraviolet Detection With Wearable and Self-Powered Halide Perovskite-Based Photodetector," *ACS applied materials & interfaces* 13 (2021): 57609–57618, https://doi.org/10.1021/acsami.1c18099.

29. J. Meier, H. Zhang, U. Kaya, W. Mertin, and G. Bacher, "Graphene-Enhanced UV-C LEDs," *Advanced Materials* 36 (2024): 2313037, https://doi.org/10.1002/adma.202313037.

30. U. Kaya, A. Sahinovic, L. Lörcher, et al., "DFT-Assisted Approach to Low-Temperature Graphene Growth on Sapphire," *Small* 21 (2025): 07332, https://doi.org/10.1002/smll.202507332.

31. K. O. Egbo, C. E. Ekuma, C. P. Liu, and K. M. Yu, "Efficient p - type Doping of Sputter-deposited NiO Thin Films With Li, Ag, and Cu Acceptors," *Physical Review Materials* 4 (2020): 104603, https://doi.org/10.1103/PhysRevMaterials.4.104603.

32. J. Hennessy, K. Balasubramanian, C. S. Moore, et al., "Performance and Prospects of Far Ultraviolet Aluminum Mirrors Protected by Atomic Layer Deposition," *Journal of Astronomical Telescopes, Instruments, and Systems* 2 (2016): 041206, https://doi.org/10.1117/1.JATIS.2.4.041206.

33. A. Mezzi and S. Kaciulis, "Surface Investigation of Carbon Films: From Diamond to Graphite," *Surface and Interface Analysis* 42 (2010): 1082–1084, https://doi.org/10.1002/sia.3348.

34. A. C. Ferrari and D. M. Basko, "Raman Spectroscopy as a Versatile Tool for Studying the Properties of Graphene," *Nature Nanotechnology* 8 (2013): 235–246, https://doi.org/10.1038/nnano.2013.46.

35. S.-E. Zhu, S. Yuan, and G. C. A. M. Janssen, "Optical Transmittance of Multilayer Graphene," *EPL (Europhysics Letters)* 108 (2014): 17007, https://doi.org/10.1209/0295-5075/108/17007.

36. F. Tuinstra and J. L. Koenig, "Raman Spectrum of Graphite," *The Journal of Chemical Physics* 53 (1970): 1126–1130, https://doi.org/10.1063/1.1674108.

37. A. F. Zatsepin, Y. Kuznetsova, and V. I. Sokolov, "UV Absorption and Effects of Local Atomic Disordering in the Nickel Oxide Nanoparticles," *Journal of Luminescence* 183 (2017): 135–142, https://doi.org/10.1016/j.jlumin.2016.11.006.

38. M. Tyagi, V. B. Raj, and M. Tomar, "High Gain NiO/ZnO Heterojunction Photodiodes Operated in Deep-Ultraviolet Region," *Thin Solid Films* 798 (2024): 140389, https://doi.org/10.1016/j.tsf.2024.140389.

39. S. Wrede, Q. Liu, L. Chen, et al., "Insights Into the Surface of Mesoporous Nickel Oxide and Its Interaction With Oxygen and Water," *Physical Chemistry Chemical Physics* 27 (2025): 12762–12773, https://doi.org/10.1039/d5cp00137d.

40. R. Al-Gaashani, S. Radiman, A. R. Daud, N. Tabet, and Y. Al-Douri, "XPS and Optical Studies of Different Morphologies of ZnO Nanostructures Prepared by Microwave Methods," *Ceramics International* 39 (2013): 2283–2292, https://doi.org/10.1016/j.ceramint.2012.08.075.

41. J. Zuo and A. Erbe, "Optical and Electronic Properties of Native Zinc Oxide Films on Polycrystalline Zn," *Physical Chemistry Chemical Physics* 12 (2010): 11467–11476, https://doi.org/10.1039/c004532b.

42. K. O. Egbo, C. P. Liu, C. E. Ekuma, and K. M. Yu, "Vacancy Defects Induced Changes in the Electronic and Optical Properties of NiO Studied by Spectroscopic Ellipsometry and First-principles Calculations," *Journal of Applied Physics* 128 (2020): 135705, https://doi.org/10.1063/5.0021650.

43. R. Bujdák, M. Derzsi, and K. Tokár, "Identity of Oxygen-Rich Nickel Oxides as Oxosuperoxides and Oxoperoxides and Their Heterostructures," *Inorganic Chemistry* 64 (2025): 15402–15412, https://doi.org/10.1021/acs.inorgchem.5c01477.

44. M. Ono, K. Sasaki, H. Nagai, et al., "Relation between Electrical and Optical Properties of p-Type NiO Films," *Physica Status Solidi* 255 (2018): 1700311, https://doi.org/10.1002/pssb.201700311.

45. M. C. Li, M. J. Dai, S. S. Lin, et al., "Effect of Annealing Temperature on the Optoelectronic Properties and Structure of NiO Films," *Ceramics International* 48 (2022): 2820–2825, https://doi.org/10.1016/j.ceramint.2021.10.071.

46. B. Pandit, B. Parida, H.-S. Jang, and K. Heo, "Self-Powered Broadband Photodetector Based on NiO/Si Heterojunction Incorporating Graphene Transparent Conducting Layer," *Nanomaterials* 14 (2024): 551, https://doi.org/10.3390/nano14060551.

47. S. J. Ikhmayies, A. El-Haija, M. N, and R. N. Ahmad-Bitar, "A Comparison Between Different Ohmic Contacts for ZnO Thin Films," *Journal of Semiconductors* 36 (2015): 033005, https://doi.org/10.1088/1674-4926/36/3/033005.

48. S. B. Tekin, S. Almalki, H. Finch, et al., "Electron Affinity of Metal Oxide Thin Films of TiO_2, ZnO, and NiO and Their Applicability in 28.3 THz Rectenna Devices," *Journal of Applied Physics* 134 (2023): 084503, https://doi.org/10.1063/5.0157726.

49. Y. Zhang, J. Zuo, Y. Gao, P. Li, W. He, and Z. Zheng, "Investigation on the Nanoscale Electric Performance of NiO Thin Films by C-AFM and KPFM: The Effect of Cu Doping," *Journal of Physics and Chemistry of Solids* 131 (2019): 27–33, https://doi.org/10.1016/j.jpcs.2019.03.013.

50. K. Cheng, N. Han, Y. Su, J. Zhang, and J. Zhao, "Schottky Barrier at Graphene/Metal Oxide Interfaces: Insight From First-Principles Calculations," *Scientific Reports* 7 (2017): 41771, https://doi.org/10.1038/srep41771.

51. D. Belotcerkovtceva, R. P. Maciel, E. Berggren, et al., "Insights and Implications of Intricate Surface Charge Transfer and sp3-Defects in Graphene/Metal Oxide Interfaces," *ACS Applied Materials & Interfaces* 14 (2022): 36209–36216, https://doi.org/10.1021/acsami.2c06626.

52. J. Meyer, P. R. Kidambi, B. C. Bayer, et al., "Metal Oxide Induced Charge Transfer Doping and Band Alignment of Graphene Electrodes for

21951071, 0, Downloaded from https://advanced.onlinelibrary.wiley.com/doi/10.1002/adom.71412 by Universitaet Duisburg-Essen, Wiley Online Library on [02/07/2026]. See the Terms and Conditions (https://onlinelibrary.wiley.com/terms-and-conditions) on Wiley Online Library for rules of use; OA articles are governed by the applicable Creative Commons License

Efficient Organic Light Emitting Diodes," *Scientific Reports* 4 (2014): 5380, https://doi.org/10.1038/srep05380.

53. H. Yang, G. H. Guai, C. Guo, et al., "NiO/Graphene Composite for Enhanced Charge Separation and Collection in p-Type Dye Sensitized Solar Cell," *The Journal of Physical Chemistry C* 115 (2011): 12209–12215, https://doi.org/10.1021/jp201178a.

54. N. Wang, Y. Liu, M. Li, J. Zhao, X. Zhang, and D. Jiang, "Self-Powered p-NiO/n-ZnO Heterojunction Ultraviolet Photodetector Based on Honeycomb Nano-Mesh Structure," *Sensors* 24 (2024): 7733, https://doi.org/10.3390/s24237733.

55. P. Salunkhe, P. Bhat, and D. Kekuda, "Performance Evaluation of Transparent Self-powered n-ZnO/p-NiO Heterojunction Ultraviolet Photosensors," *Sensors and Actuators A: Physical* 345 (2022): 113799, https://doi.org/10.1016/j.sna.2022.113799.

56. C. Wei, J. Xu, S. Shi, et al., "The Improved Photoresponse Properties of Self-powered NiO/ZnO Heterojunction Arrays UV Photodetectors With Designed Tunable Fermi Level of ZnO," *Journal of Colloid and Interface Science* 577 (2020): 279–289, https://doi.org/10.1016/j.jcis.2020.05.077.

57. N. P. Klochko, "Semi-transparent UV Photodetectors Based on the Nanostructured n-ZnO/p-CuI and n-ZnO/p-NiO Diode Heterojunctions Prepared by Low Temperature Solution Growth," in *2018 IEEE 8th International Conference Nanomaterials: Application & Properties (NAP)* September 9, 2018, 1–5.

58. Y. Luo, Z. Dong, Y. Chen, et al., "Self-Powered NiO@ZnO-Nanowire-Heterojunction Ultraviolet Micro-Photodetectors," *Optical Materials Express* 9 (2019): 2775, https://doi.org/10.1364/OME.9.002775.

59. B. Li, P. Xie, B. Chen, et al., "Electrode-Dependent and Tunable Sub-to-Super-Linear Responsivity in Mott Material-Enabled Near-Infrared Photodetectors for Advanced Near-Sensor Image Processing," *Advanced Materials* 36 (2024): 2410952, https://doi.org/10.1002/adma.202410952.

60. C. Soci, A. Zhang, B. Xiang, et al., "ZnO Nanowire UV Photodetectors With High Internal Gain," *Nano Letters* 7 (2007): 1003–1009, https://doi.org/10.1021/nl070111x.

61. P. M. Wojcik, L. D. Bastatas, N. Rajabi, P. V. Bakharev, and D. N. McIlroy, "The Effects of Sub-Bandgap Transitions and the Defect Density of States on the Photocurrent Response of a Single ZnO-Coated Silica Nanospring," *Nanotechnology* 32 (2021): 035202, https://doi.org/10.1088/1361-6528/abbcec.

62. L. Liu, Z. Mei, A. Tang, et al., "Oxygen Vacancies: The Origin of n-Type Conductivity in ZnO," *Physical Review B* 93 (2016): 235305, https://doi.org/10.1103/PhysRevB.93.235305.

63. J. Klein, L. Kampermann, B. Mockenhaupt, M. Behrens, J. Strunk, and G. Bacher, "Limitations of the Tauc Plot Method," *Advanced Functional Materials* 33 (2023): 2304523, https://doi.org/10.1002/adfm.202304523.

64. L. Grebener, Y. Jarrahizadeh, S. Pourdahrany, et al., "Colloidal Dispersions of Substrate-free Gas-Phase Synthesized Graphene: Dispersion Formulation for Thin Film Formation," *Carbon* 252 (2026): 121365, https://doi.org/10.1016/j.carbon.2026.121365.

65. S. M. Sze and K. K. Ng, *Physics of Semiconductor Devices*, 3rd ed. (Wiley, 2006), https://doi.org/10.1002/0470068329.

Supporting Information

Additional supporting information can be found online in the Supporting Information section.

Supporting File: adom71412-sup-0001-SuppMat.docx.

21951071, 0, Downloaded from https://advanced.onlinelibrary.wiley.com/doi/10.1002/adom.71412 by Universitaet Duisburg-Essen, Wiley Online Library on [02/07/2026]. See the Terms and Conditions (https://onlinelibrary.wiley.com/terms-and-conditions) on Wiley Online Library for rules of use; OA articles are governed by the applicable Creative Commons License